IOPscience iopscience.iop.org

Home Search Collections Journals About Contact us My IOPscience

Measurement of doubly differential electron bremsstrahlung cross sections at the end point (tip) for C, Al, Te, Ta and Au

This content has been downloaded from IOPscience. Please scroll down to see the full text.

2017 J. Phys. B: At. Mol. Opt. Phys. 50 155003

(http://iopscience.iop.org/0953-4075/50/15/155003)

View the table of contents for this issue, or go to the journal homepage for more

Download details:

IP Address: 200.130.19.195
This content was downloaded on 28/08/2017 at 17:35

Please note that terms and conditions apply.

You may also be interested in:

Ionization cross sections of the L subshells of Au by 50 to 100 keV electron impact
S F Barros, V R Vanin, N L Maidana et al.

Cross sections of K-shell ionization by electron impact, measured from threshold to 100 kev, for Au and Bi
J M Fernández-Varea, V Jahnke, N L Maidana et al.

Two-parameter coincidence measurements of bremsstrahlung, electron-electron bremsstrahlung, and K-shell ionisation for 300 keV electron impact
M Komma and W Nakel

K-shell ionizationby electrons
X Llovet, C Merlet and F Salvat

Overview of physical interaction models for photon and electron transport used in Monte Carlo codes
Francesc Salvat and José M Fernández-Varea

Design for transmission x-ray tubes
L M N Távora, E J Morton and W B Gilboy

Spectral shapes for atomic-field bremsstrahlung produced by beta particles of yttrium-90 in thick targets of Cu. Cd, Ta and Pb
Shivaramu

Uncertainties in gamma-ray spectrometry
M C Lépy, A Pearce and O Sima

IOP Publishing Journal of Physics B: Atomic, Molecular and Optical Physics

J. Phys. B: At. Mol. Opt. Phys. **50** (2017) 155003 (14pp) https://doi.org/10.1088/1361-6455/aa7ac4

Measurement of doubly differential electron bremsstrahlung cross sections at the end point (tip) for C, Al, Te, Ta and Au

J A García-Alvarez[1,2,5], J M Fernández-Varea[3,1], V R Vanin[1], O C B Santos[1], S F Barros[1], A A Malafronte[1], C L Rodrigues[1], M N Martins[1], M F Koskinas[4] and N L Maidana[1]

[1] Instituto de Física, Universidade de São Paulo. Rua do Matão 1371, Cidade Universitária, CEP: 05508-090, São Paulo, SP, Brazil
[2] Instituto Superior de Tecnologías y Ciencias Aplicadas, Universidad de La Habana. Quinta de los Molinos, Ave. Salvador Allende, Esq. Luaces, Plaza, CP:10400 La Habana, Cuba
[3] Facultat de Física (FQA and ICC), Universitat de Barcelona. Diagonal 645, E-08028 Barcelona, Spain
[4] Instituto de Pesquisas Energéticas e Nucleares (IPEN/CNEN-SP). Av. Prof. Lineu Prestes 2242, Cidade Universitária, CEP: 05508-000, São Paulo, SP, Brazil

E-mail: jale@if.usp.br and jagarcia@instec.cu

Received 5 May 2017, revised 15 June 2017
Accepted for publication 21 June 2017
Published 7 July 2017

Abstract

We have used the low-energy beam line of the São Paulo Microtron accelerator to study the maximum energy transfer point (tip) of electron–atom bremsstrahlung spectra for C, Al, Te, Ta and Au. Absolute cross sections differential in energy and angle of the emitted photon were measured for various electron kinetic energies between 20 and 100 keV, and photon emission angles of 35°, 90° and 131°. The bremsstrahlung spectra were collected with three HPGe detectors and their response functions were evaluated analytically. Rutherford backscattering spectrometry allowed us to obtain the thicknesses of the targets with good accuracy. We propose a simple model for the tip region of the bremsstrahlung spectrum emitted at a given angle, whose adjustable parameters are the mean energy of the incident beam and its spread as well as an amplitude. The model was fitted simultaneously to the pulse-height distributions recorded at the three angles, determining the doubly differential cross sections from the corresponding amplitudes. The measured values have uncertainties between 3% and 13%. The agreement of the experimental results with the theoretical partial-wave calculations of Pratt and co-workers depends on the analyzed element and angle but is generally satisfactory. In the case of Al and Au, the uncertainty attributed to the theory is probably overestimated.

Keywords: electron–atom bremsstrahlung, end point, cross section

(Some figures may appear in colour only in the online journal)

1. Introduction

The high-frequency end point of a bremsstrahlung spectrum, usually called the spectrum 'tip', corresponds to interactions in which the kinetic energy of the incident electron is totally radiated. This part of the energy distribution has been of special theoretical interest since the beginning of the bremsstrahlung theory development [1–11], mainly motivated by the well-known limitations of the Bethe–Heitler formula [12] derived in the Born approximation.

A very fruitful idea was introduced by Fano *et al* [1] resorting to the 'detailed balance' between photoelectric effect and bremsstrahlung emission in the high-frequency limit. In a series of works, Pratt and co-workers [2, 3, 5, 8, 9, 11] refined this proposal in order to predict the bremsstrahlung cross section (differential in the energy of the

---

[5] Author to whom any correspondence should be addressed.

emitted photon) at the end point from the most accurate theoretical photoeffect cross sections. The photoeffect and bremsstrahlung emission cross sections can be related only at the same photon energy, hence it is assumed that the difference in electron energies is small [2], and the treatment is not valid for electrons with kinetic energies of the order of the binding energies.

From another perspective, Elwert and Haug [6] deduced an analytical formula for the triply differential cross section having recourse to Sommerfeld–Maue continuum wave functions. In general, when this formalism is applied to the tip of the spectrum and the ensuing cross sections are compared to the previous calculations by Jabbur and Pratt [3], the authors found agreement only for low atomic numbers.

For electrons with kinetic energy E_0 between 1 and 2 MeV, the partial-wave methodology, implemented by Tseng and Pratt [13] for the first time, constitutes the state of the art for the calculation of electron–nucleus bremsstrahlung cross sections. This approach treats the photon emission as a one-electron transition in a relativistic self-consistent screened atomic potential. The main quantities tabulated using this formalism were the cross section $\mathrm{d}\sigma/\mathrm{d}E$ differential in the photon energy E [14] and the bremsstrahlung shape function S (the photon angular distribution) [15]. Details on the numerical procedures can be consulted in [16, 17]. Later on, Seltzer and Berger [18, 19] prepared another tabulation of differential cross sections, extending the electron kinetic energy to 10 GeV. To this end they adopted several theories depending on E_0, and included in $\mathrm{d}\sigma/\mathrm{d}E$ a component that accounts for the bremsstahlung emitted in the field of the atomic electrons. In the interval 1 keV $\leqslant E_0 \leqslant$ 2 MeV the data of Seltzer and Berger [19] are essentially the partial-wave cross sections calculated by Pratt *et al* [14].

The tabulations of Pratt *et al* [14] and Kissel *et al* [15] are regarded as the most authoritative theoretical description of the energy and angular photon distributions, respectively, of ordinary bremsstrahlung. They cover atomic numbers $1 \leqslant Z \leqslant 92$ and all the radiated photon energies $0 \leqslant \kappa \leqslant 1$, where $\kappa \equiv E/E_0$ is the reduced photon energy, for the interval of electron energies 1 keV $\leqslant E_0 \leqslant$ 2 MeV. The data were obtained by interpolation/extrapolation in a sparse set of 144 calculated cases, namely $Z = 2$, 8, 13, 47, 79 and 92, $E_0 = 1$, 5, 10, 50, 100, 500, 1000 and 2000 keV[†], and $\kappa = 0$, 0.4, 0.6 and 0.95 [16, 17]. The values at the end point $\kappa = 1$ were deduced by extrapolation [16]. Combining both tabulations and for given values of Z, E_0, κ and θ, the doubly differential cross section (DDCS) $\mathrm{d}^2\sigma/\mathrm{d}E\mathrm{d}\Omega$ can be computed from the product $(\mathrm{d}\sigma/\mathrm{d}E)S$ [15], see equation (3) below.

In fact, the DDCS is the most studied quantity in the experimental context [20, 21]. However, experiments intended to yield the DDCS at the end point are scarce. To our knowledge, the DDCS at $\kappa = 1$ were measured in only two occasions. The first experiment was conducted by Starek, Aiginer and Unfried [22], for incident electrons of 1.84 MeV in targets of Li, Al, Cu, Ag, Au and Pb, and the photon emission angle $\theta = 10°$. To collect the bremsstrahlung spectra the authors used a coaxial Ge(Li) detector and established its response function (RF) with an ^{88}Y radioactive source [22]. The thicknesses of the targets were measured, as they were being manufactured by evaporation, employing the frequency shift of a quartz crystal oscillator. The uncertainties of the absolute DDCSs reported by Starek *et al* [22] are between 2% and 3%.

These measurements prompted Pratt and Tseng [8] to make a comparison with different theories. They calculated the DDCS for the same physical variables of the experiment applying the analytical formulation of Elwert and Haug, the exact partial-wave framework, and the connection between the tip of the bremsstrahlung spectrum and the atomic photoeffect [8]. In this respect, for medium- and high-Z elements (Cu, Ag, Au and Pb) Pratt and Tseng found fairly good accord between the second and third of these theories and experiment [8]. Nevertheless, for low-Z elements (Li and Al) there was poor agreement between experiment and theory.

The second experiment was performed by Aehlig, Sheer and Zilker [23], studying four electron kinetic energies in the interval 100–250 keV, in two targets of Cu, and two photon emission angles: $\theta = 25°$ and 50°. To determine the DDCS at $\kappa = 1$, simultaneously with the detected photons in a Ge(Li) spectrometer they counted the elastically scattered electrons collected with a surface barrier detector [23]. This relative method circumvents the need to know the thickness of the targets using instead theoretical elastic-scattering cross sections to place the DDCSs on an absolute scale. The experiment aimed at testing the validity of the Elwert–Haug formalism [6, 7] for medium-Z elements. Aehlig *et al* [23] found that, on average, their measured data were somewhat higher than the theoretical Elwert–Haug DDCSs, but the discrepancy did not exceed 20%.

The present article describes the methodology that we followed to measure the absolute DDCS at $\kappa = 1$, for various (at least four) electron kinetic energies E_0 between 20 and 100 keV, in targets of C, Al, Te, Ta and Au, and three photon emission angles: $\theta = 35°$, 90° and 131°. Our study explores a range of electron kinetic energies where experimental data are not available. Furthermore, in this interval the theoretical DDCSs are affected by a large relative uncertainty (11%), associated to the combined contributions of the differential cross section $\mathrm{d}\sigma/\mathrm{d}E$ (10%) tabulated by Seltzer and Berger [19], and the bremsstrahlung shape function S (5%) of Kissel *et al* [15]. These uncertainties arise chiefly from the choice of the atomic potential and the limited number of terms in the partial-wave expansion. As already mentioned, in these tabulations the data at $\kappa = 1$ were generated by extrapolation from the partial-wave calculations of both quantities at the values $\kappa = 0.4$, 0.6 and 0.95 [16–18]. Besides testing the extrapolation in the variable κ, our experiment allows to examine the interpolation procedure in E_0 and Z. Recall that for 20 keV $\leqslant E_0 \leqslant$ 100 keV and $6 \leqslant Z \leqslant 79$ the aforementioned tabulations contain only twelve points where partial-wave cross sections were actually calculated (see

---

[†] The bremsstrahlung shape function was tabulated only up to $E_0 = 500$ keV.

above); the values at any other combination of E_0 and Z had to be obtained by interpolation.

The synthetic databases of Seltzer and Berger [19] and Kissel *et al* [15] are implemented in several general-purpose Monte Carlo codes (e.g. GEANT4 [24], EGSnrc [25] and PENELOPE [26]) to simulate bremsstrahlung energy and angular distributions. The application of Monte Carlo simulations in many fields, like medical physics, demands a thorough validation of these tables, as remarked in [27, 28].

The rest of the paper is structured as follows. Section 2 describes the experimental setup, including the targets, the electron beam, the irradiation chamber (IC), the detectors and their RFs. The analysis of the collected data is depicted in section 3. The measured cross sections are presented in section 4, where they are compared with the theoretical predictions, and the discussion is provided in section 5. Finally, the conclusions are drawn in section 6. Two appendices are added to avoid cluttering the main text, one to describe a simplified model for the detector RF and another to outline the calculation of the increment in the solid angle subtended by the detectors with respect to the irradiation point.

2. Experimental setup

2.1. Target preparation and characterization

Two types of thin targets were used in this work: either a single film of C or films composed of two layers, one of the elements Al, Te, Ta or Au, and another of C. The C film serves as a substrate for the other materials. In a first step, C films were mounted on 15 × 30 mm^2 rectangular frames of carbon fiber, 0.3 mm thick, having a 10 mm circular opening in its center. Films of Al, Te, Ta and Au were subsequently deposited by magnetron sputtering over those C substrates. During the evaporation, a mask of steel was placed in front of the frames, limiting the deposited elements to a circular area of 8 mm in diameter. Throughout the text we will denote these targets as X/C, where X indicates the element of interest and *C* the substrate.

Rutherford backscattering spectrometry (RBS) was applied to characterize the targets. The measurements were done at the LAMFI/IFUSP tandem van de Graaff accelerator [29], employing a 2200 keV ^{4}He$^+$ beam and a Si surface barrier detector placed at the scattering angle of 120°. From the collected RBS spectra we deduced the number of atoms per unit surface $\mathcal{N}t$ ($\mathcal{N}$ is the number of atoms per unit volume and t the thickness of each layer) using the MultiSIMNRA program [30], which is based on SIMNRA calculations [31]. Table 1 summarizes the values of $\mathcal{N}t$ and t, the latter calculated with bulk mass densities. An example of a typical RBS spectrum pertaining to the Au/C target and the corresponding MultiSIMNRA/SIMNRA fit are shown in figure 1. It can be observed that there is no extended tail at the left side of the peaks corresponding to elastic backscattering in the C and the Au layers. From this evidence we conclude that both layers present a uniform thickness distribution [31]. Similar behaviors were found in all the RBS spectra. The smallness of the peaks in the vicinity of 950 keV confirms that the oxidation of the target is negligible.

Table 1. Atomic areal densities and thicknesses of the targets as determined by RBS. The numbers between parentheses are the uncertainties (one standard deviation) in units of the least significant digit.

	$\mathcal{N}t$ (10^{15} at cm^{-2})		t (nm)	
Target	Element	C substrate	Element	C substrate
C	450(23)	—	39.6(20)	—
Al/C	100(4)	562(20)	16.6(7)	49.4(18)
Te/C	110(3)	525(10)	37.4(11)	46.2(9)
Ta/C	60.6(24)	461(10)	11.2(4)	40.6(9)
Au/C	29.9(6)	610(20)	5.07(10)	53.7(18)

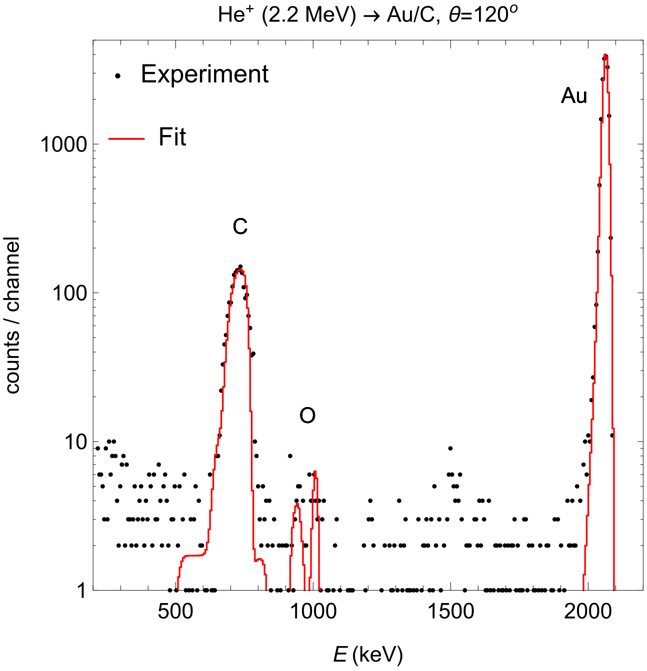

Figure 1. RBS spectrum of the Au/C target (dots) and MultiSIMNRA/SIMNRA fit (continuous curve). The narrow peak centered at 2065 keV corresponds to the elastic backscattering of the incident projectiles in the Au layer, whereas the structure around 715 keV characterizes the same effect in the C substrate.

2.2. Electron beam and IC

The measurements of the electron bremsstrahlung DDCSs were carried out at the low-energy beam line of the São Paulo Microtron accelerator. In this beam line, the electrons emitted by the accelerator gun with kinetic energy between 10 and 100 keV are deflected by a dipole magnet towards the IC.

The IC consists of an electrically isolated cylindrical structure with stainless steel side walls, upper and lower Al caps, with an internal diameter of 490 and 220 mm in height (see figure 2). Several 50 μm thick duralumin spectroscopy windows allow for the collection of bremsstrahlung photons at different angles θ_i with respect to the incident beam direction ($\theta = 0°$). On the opposite side of the point that defines the entrance of the electrons to the IC there is a

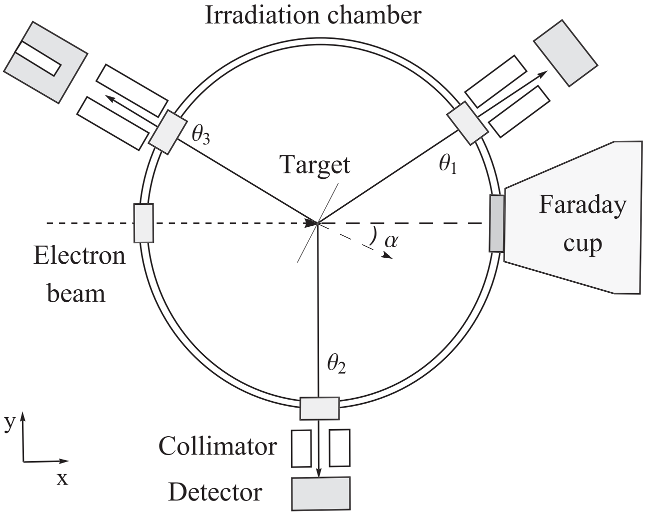

Figure 2. Two-dimensional scheme of the IC (not to scale), illustrating the positions of the HPGe detectors.

conical graphite Faraday cup whose design minimizes the backscattering of electrons to the IC and the emission of unwanted bremsstrahlung. For the energy interval of the incoming electrons, this device catches a significant fraction of the beam after crossing the target. In fact, this fraction corresponds to 65% for the Au film at 20 keV and more than 95% at 100 keV. Two current integrators connected respectively to the IC and to the Faraday cup fully collect the incident electrons.

The sample holder is made of carbon fiber and it can accommodate six targets. It is positioned along the symmetry axis of the cylindrical IC and can be moved vertically without breaking the vacuum or varying the energy of the electron beam. Since the targets consist of a low-Z substrate plus the element of interest (see above), the collection of spectra with the same electron kinetic energy is essential for the subsequent correction of substrate effects (see section 2.5). For the measurements presented here the holder was rotated by an angle $\alpha = 30°$ between the direction normal to the target surface and the electron beam (figure 2). As a consequence, the effective path of the electrons in the target is $t/\cos\alpha$. The base pressure in the IC was 0.1 mPa.

2.3. X-ray detection arrangement

The x-ray spectra were collected with three ORTEC HPGe detectors (ORTEC Advanced Measurements Technology, Oak Ridge, USA). At the angle $\theta_1 = 35°$ with respect to the electron beam incident direction, was placed a planar detector, GLP Series, with thickness and radius of the Ge active volume of 7.3 mm and 16 mm, respectively, and a Be window of 0.254 mm (figure 2). A DSPEC digital spectrometer was coupled to this detector. At $\theta_2 = 90°$ was located another planar detector (1000 Series), whose Ge crystal has a thickness of 10 mm, a radius of 12.5 mm and a Be window of 0.25 mm. In this case, the spectrometric chain included an ORTEC 572 amplifier and a multichannel analyzer ASPEC 927. The third detector, positioned at $\theta_3 = 131°$, is a coaxial HPGe model GMX30P4-70-CW-SMN. Its crystal has 66.3 mm in length and 58 mm in diameter, with an internal hole 10 mm in diameter and 58 mm in depth. The detector window is made of carbon fiber and it has a thickness of 0.9 mm. A DSPEC-Jr 2.0 digital spectrometer was coupled to this detector.

Three cylindrical Cu collimators with 10 mm of aperture and length of 100 mm (for the positions θ_1 and θ_3), and 70 mm (for θ_2), were placed between the frontal surfaces of the detectors and the spectroscopy windows outside the IC (figure 2). After careful alignment with each of the Ge crystal axes and the target position, the collimators ensure that photons reach the detectors under narrow solid angles ($\Omega \sim 5 \times 10^{-4}$ sr). In this situation, the angular variation $\Delta\theta$ of θ within Ω is less than 2°. Therefore, the DDCS is well approximated by a linear function of θ so that the mean value of the DDCS in the interval $\Delta\theta$ coincides with the value at the central point (in our case $\theta_1 = 35°$, $\theta_2 = 90°$ and $\theta_3 = 131°$). To reduce the natural radioactive background, the detectors were shielded around their active volumes with a layer of Cu and bricks of Pb.

2.4. RF of the Ge detectors, calibration of efficiency and energy resolution

As the bremsstrahlung spectra are continuous, for the data analysis it is essential to know the RF of each detector. The RF $R(h, E)$ is the probability density that a photon of energy E produces a pulse of height h in a multichannel histogram. We started from the methodology described in [32] to evaluate $R(h, E)$. This analytical RF model is valid for planar Ge detectors and normal incidence of a pin-hole collimated photon beam with energies between 10 and 100 keV. The RF is

$$R(h, E) = T(E)\int_0^\infty \mathcal{G}(h, \epsilon; s)\, D(\epsilon, E; \mathbf{g})\, \mathrm{d}\epsilon, \qquad (1)$$

where $T(E)$ is the fraction of photons transmitted through the materials in front of the active volume, $D(\epsilon, E; \mathbf{g})$ is the probability density that a photon with energy E deposits an energy ϵ in the active volume and the Gaussian distribution $\mathcal{G}(h, \epsilon; s)$ models the probability that the deposited energy ϵ gives rise to a pulse of height h [32]. The RF model only requires as input data (1) the detector geometrical parameters $\mathbf{g}$ (length and radius of the Ge active volume, thicknesses of the Ge dead layer and the detector window, etc), and (2) the coefficients a and b that describe the energy dependence of the variance $s^2 = a + b\epsilon$ in $\mathcal{G}(h, \epsilon; s)$ (typically deduced from FWHM calibrations) [32]. The mathematical expression for $D(\epsilon, E; \mathbf{g})$ developed in [32] can be simplified substantially if we limit ourselves to analyze the *tip* region of the bremsstrahlung spectra; the reader is referred to appendix A for a complete description of the adopted RF.

In order to determine the absolute full-energy peak efficiency $\varepsilon_\mathrm{a}(E)$ and also to calibrate the energy resolution of the detectors, we measured spectra from radioactive sources of ^{133}Ba (two), ^{152}Eu (one) and ^{241}Am (two) with certified activities. The sources were manufactured for this work at LMN-IPEN/CNEN-SP (Nuclear Metrology Laboratory, Institute of Nuclear Research, National Commission for

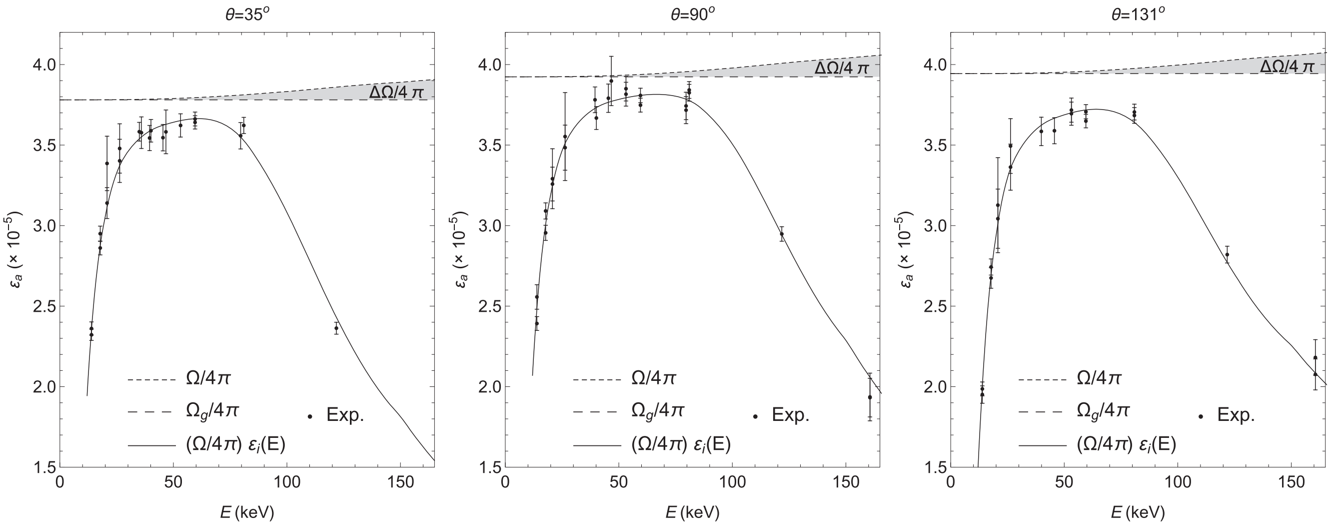

Figure 3. Absolute full-energy peak efficiencies of the HPGe detectors. The circles with error bars (one standard deviation) are experimental values. The continuous curves were calculated with equation (23) of [32]. The fitted geometrical efficiencies, $\Omega_g/4\pi$, are represented as dashed horizontal lines. The shaded areas are $\Delta\Omega(E)/4\pi$, the increase in the fraction of solid angle as a result of the collimator transparency.

Nuclear Energy, São Paulo) with the same geometry as the targets. This means that kapton films were mounted on carbon fiber frames equal to those described in section 2.1, the radioactive material was deposited over the films and finally covered by another kapton film. The sources were placed in the sample holder for these calibrations.

Since the absolute and intrinsic efficiencies are linearly related through $\varepsilon_a(E) = (\Omega/4\pi)\varepsilon_i(E)$, using the efficiency values measured with the radioactive sources and the modeled ε_i, we fitted the fraction of solid angle $(\Omega/4\pi)$, which represents the geometric efficiency (see figure 3). We accounted for the increment of solid angle $\Delta\Omega(E)$ caused by the partial transparency of the Cu collimator for higher photon energies; the methodology is described in appendix B. This procedure allows to check experimentally the main component of the RF model and yields the solid angle subtended by each detector with respect to the target with high accuracy. Besides, using the FWHM of the full-energy peaks produced by the observed γ-rays we found for each spectrometer the parameters a and b needed to evaluate the variance s^2 of $\mathcal{G}(h, E; s)$ in the RF.

2.5. Measurement of the bremsstrahlung spectra

Bremsstrahlung spectra were collected simultaneously with the three HPGe detectors for a number of electron kinetic energies between 20 and 100 keV. The MAESTRO software (ORTEC, Oak Ridge, USA) was used to control data acquisition. In all runs we measured both the studied target X/C and the C film in order to correct for the bremsstrahlung generated in the substrate. The incident current (tens of nA) was chosen to keep the dead time of the detectors below 8%. Figure 4 displays examples of measured spectra for electrons of 51 keV. Notice that the number of electrons N_0 that impinged on the C target was about 10 times higher than in its Au/C counterpart. In general, for a given beam current the detectors observe different photon rates depending on their angular position. Hence, the number of incident electrons associated with each collected spectrum was evaluated multiplying N_0 by the respective live-time to real-time ratio.

Two main corrections had to be performed to derive the net bremsstrahlung spectrum generated by the film of the studied element. The first one is to remove, from each collected spectrum, the contributions of the natural background and pulse pile-up. These effects are particularly important in the tip region and were taken into account following the procedures described in [33, 34]. The second is to subtract from the corrected spectra of Al, Te, Ta and Au the spectrum acquired for C, renormalized by the number of incident electrons and by the number of C atoms per unit surface in each X/C target and in the C target.

3. Data analysis

3.1. Modeling the tip of the bremsstrahlung spectrum

As a consequence of the interaction of electrons with kinetic energy E_e in a thin target, the number of photons with energies between E and $E + dE$, emitted in the direction θ around a small solid angle Ω, can be calculated as

$$b(E_e;\, E) = N_0\, (\mathcal{N}t/\cos\alpha)\, \Omega\, \frac{d^2\sigma}{dE\, d\Omega}. \tag{2}$$

Introducing the scaled differential cross section $\chi(Z, E_e, E)$ [19] and the shape function $S(Z, E_e, E, \theta)$ [15], the bremsstrahlung DDCS can be written as

$$\frac{d^2\sigma}{dE\, d\Omega} = \frac{Z^2}{\beta^2}\, \frac{1}{E}\, \chi(Z, E_e, E)\, S(Z, E_e, E, \theta), \tag{3}$$

where Z is the atomic number of the target element and β is the electron velocity in units of the speed of light in vacuum. Now we substitute the DDCS of equation (3) into equation (2). The factors that do not depend on the photon energy can be

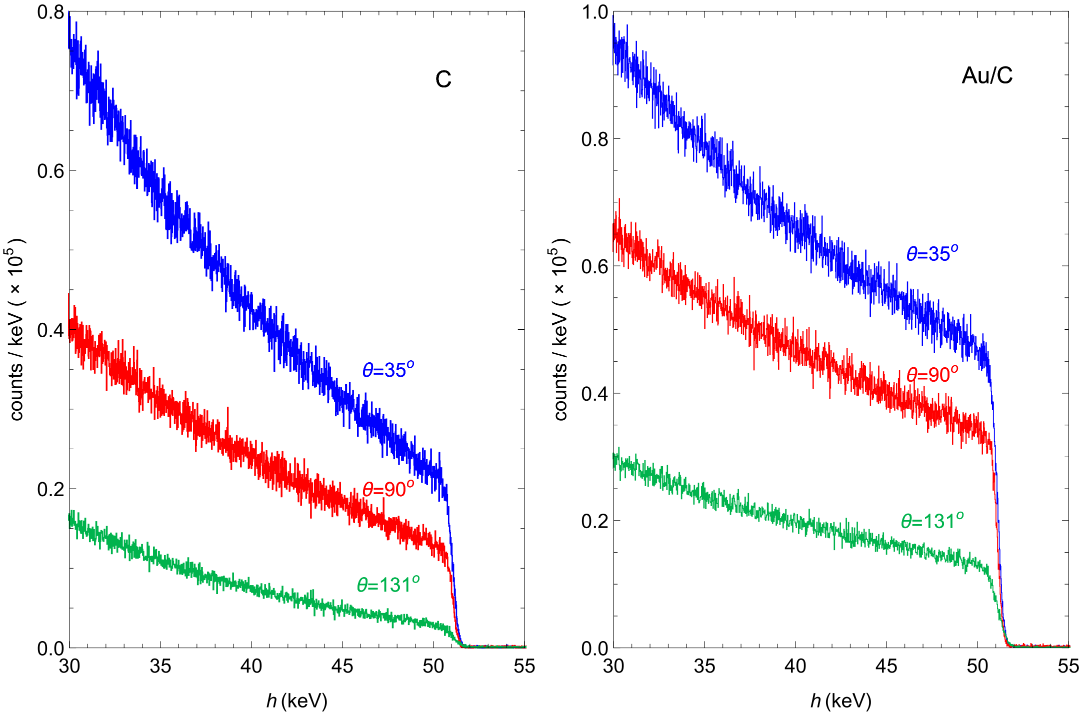

Figure 4. Pulse-height spectra collected by the three HPGe detectors for 51 keV electrons striking the C (left) and Au/C (right) targets. The dispersion is 17.8, 17.6 and 25.1 eV/channel for the detectors placed at 35°, 90° and 131°, respectively. The number of incident electrons was $N_0 = 4.180 \times 10^{16}$ for the C target and $N_0 = 5.659 \times 10^{15}$ for the Au/C target.

grouped as $C = N_0(\mathcal{N}t/\cos\alpha)\Omega\, Z^2/\beta^2$. Along the narrow energy interval ΔE where the tip of the bremsstrahlung spectrum is evaluated, we considered the dependence with E as E^{-1}. We may then introduce a constant estimator, defined by the average value $\bar{f} = \langle \chi(Z, E_e, E)\, S(Z, E_e, E, \theta)\rangle_{\Delta E}$, i.e. the variation of this product in ΔE is neglected. Notice that C and $\bar{f}$ have reciprocal dimensions. Enforcing the energy conservation principle in equation (2) through a Heaviside step function, we get a simple analytical expression to describe the bremsstrahlung tip,

$$b(E_e; E) = \frac{A}{E}\,\Theta(E_e - E), \tag{4}$$

where $A = C\bar{f}$ is a dimensionless amplitude factor that depends on E_e and θ as well as on the experimental conditions.

Strictly speaking, the electron beam coming from the gun of the accelerator is not mono-energetic. To model the energy spread it is convenient to choose a Gaussian distribution with average value E_0 and standard deviation σ_0 [33–35]. Incorporating this hypothesis into our formalism, the number of photons with energy between E and $E + \mathrm{d}E$ produced by a beam of parameters E_0 and σ_0 is given by

$$\begin{aligned} b(E_0, \sigma_0; E) &= \int_0^\infty b(E_e; E)\, \frac{1}{\sqrt{2\pi}\,\sigma_0} \\ &\quad \times \exp\left[-\frac{(E_e - E_0)^2}{2\sigma_0^2}\right]\mathrm{d}E_e \\ &= \frac{A}{2E}\left[1 + \mathrm{erf}\left(\frac{E_0 - E}{\sqrt{2}\,\sigma_0}\right)\right], \end{aligned} \tag{5}$$

which is a simple formula in terms of the error function $\mathrm{erf}(x)$. Here we assume that the amplitude parameter A experiences no significant variation during the integration, thus being regarded as a constant.

In agreement with the described formalism, the DDCS at the maximum transfer energy point can be determined by means of

$$\frac{\mathrm{d}^2\sigma}{\mathrm{d}E\,\mathrm{d}\Omega} = \frac{A/E_0}{N_0(\mathcal{N}t/\cos\alpha)\Omega}. \tag{6}$$

The ratio A/E_0 represents the number of emitted photons with $E = E_0$. The measured thicknesses t were replaced with the effective path lengths $t_{\mathrm{eff}} = c(Z, E_0)t$ of the electrons in the films of the studied elements. The correction factors $c(Z, E_0)$, obtained from Monte Carlo simulations (PENELOPE code [26]), varied between 1.00 and 1.08. In this work, we tested the proposed model for the tip of the bremsstrahlung spectrum by fitting the parameters A, E_0 and σ_0 to the measured pulse-height distributions.

3.2. Least-squares fit procedure

The probability density function $N(h)$ that describes the collection of pulses of height between h and $h + \mathrm{d}h$ in a multichannel histogram is given by the convolution of $b(E_0, \sigma_0; E)$ and the RF, i.e.

$$N(h) = \int_0^\infty R(h, E)\, b(E_0, \sigma_0; E)\, \mathrm{d}E = A\, B(E_0, \sigma_0; h) \tag{7}$$

with

$$B(E_0,\,\sigma_0;\,h)=\int_0^{\infty}R(h,\,E)\,\frac{1}{2E}\left[1+\mathrm{erf}\left(\frac{E_0-E}{\sqrt{2}\,\sigma_0}\right)\right]\mathrm{d}E. \tag{8}$$

In an experiment, the number of counts N_i in channel i corresponds to the integral of equation (7) over the channel width δ. According to our model, this number can be estimated as

$$N_i^{\mathrm{model}}=\int_{h_i-\delta/2}^{h_i+\delta/2}N(h)\,\mathrm{d}h\approx\delta\,A\,B(E_0,\,\sigma_0;\,h_i) \tag{9}$$

with h_i denoting the center of channel i. Notice that N_i^{model} is linear in A and nonlinear in the variables E_0 and σ_0 in $B(E_0,\,\sigma_0;\,h_i)$.

The least-squares fit of the beam's average energy and spread was performed minimizing the merit function

$$Q(E_0,\,\sigma_0;\,\widehat{\mathbf{A}})=\sum_{j=1}^{3}\sum_{i}\frac{[N_{j,i}-N_{j,i}^{\mathrm{model}}]^2}{\mathrm{var}(N_{j,i})}, \tag{10}$$

where $N_{j,i}$ is the number of counts in the ith channel of the spectrum registered by detector j, and $\mathrm{var}(N_{j,i})$ is its associated variance.

To evaluate the bidimensional function Q at a given coordinate pair $(E_0',\,\sigma_0')$, the three amplitude parameters $\widehat{\mathbf{A}'}=\{\widehat{A'}_j\}$ were obtained beforehand by means of the least-squares method

$$\widehat{A'}_j(E_0',\,\sigma_0')=(\mathbf{X}^{\mathrm{t}}\,\mathbf{V}^{-1}\,\mathbf{X})_j^{-1}\,(\mathbf{X}^{\mathrm{t}}\,\mathbf{V}^{-1})_j\,\mathbf{N}_j, \tag{11}$$

which represent the lower variance estimators of the set $\widehat{\mathbf{A}'}$. In equation (11), the column vector $\mathbf{N}_j$ is composed by the counts $N_{j,i}$, whereas the elements of the design matrix $\mathbf{X}_j$ and the variance matrix $\mathbf{V}_j$ are, respectively,

$$X_{j,i}=\frac{\partial N_{j,i}^{\mathrm{model}}}{\partial A_j}=\delta_j\,B(E_0',\,\sigma_0';\,h_{j,i})\quad\text{and}$$
$$V_{j,ik}=\mathrm{var}(N_{j,k})\,\delta_{i,k}. \tag{12}$$

The Kronecker delta $\delta_{i,k}$ defines $\mathbf{V}_j$ as a diagonal matrix. The variance of $\widehat{A'}_j(E_0',\,\sigma_0')$ is given by the product $(\mathbf{X}^{\mathrm{t}}\,\mathbf{V}^{-1}\,\mathbf{X})_j^{-1}$. The pair $(\widehat{E}_0,\,\widehat{\sigma}_0)$ denotes the values that minimize Q and were adopted as fitted parameters as well as the associated set $\widehat{A}_j(\widehat{E}_0,\,\widehat{\sigma}_0)$.

In all the analyzed cases, the fitting procedure of the tip region was done selecting an energy interval $\Delta E=2$ keV centered at the half height of the tip. This narrow interval ensures that the hypothesis taken for modeling the tip of the emitted spectra is valid, as described in section 3.1.

Choosing the run case example of figure 4 (Au/C target, 51 keV electrons), figure 5 presents the level curves of the corresponding merit function Q for the fit of the beam parameters E_0 and σ_0 and the set of amplitudes $\widehat{\mathbf{A}}$. As mentioned in [33, 34], Q is approximately distributed like a chi-square and in this case the minimum $Q(\widehat{E}_0,\,\widehat{\sigma}_0;\,\widehat{\mathbf{A}})=\chi^2=301$, with 293 degrees of freedom, having a 36% probability of being exceeded. The measured spectra and those calculated with the fitted values are exhibited in figure 6. Similar statistical behaviors were observed in all recorded spectra.

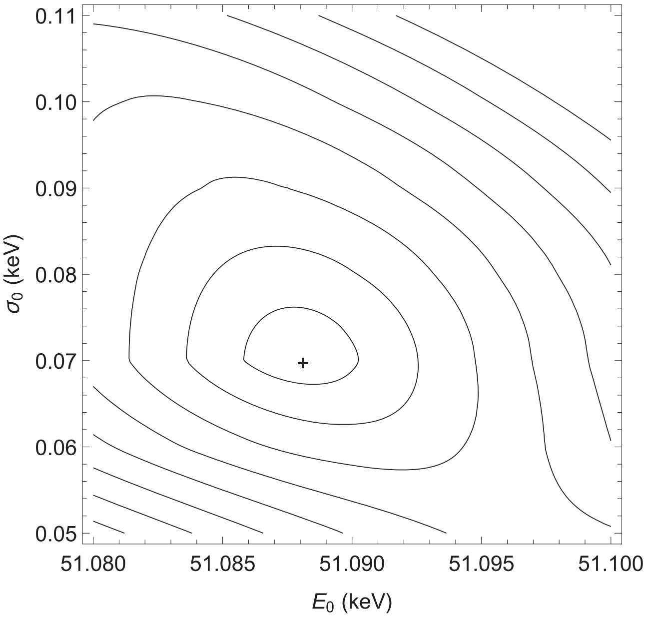

Figure 5. Level curves of the merit function Q for the Au/C target, 51 keV run. The plus symbol is located at the minimum $Q(\widehat{E}_0,\,\widehat{\sigma}_0;\,\widehat{\mathbf{A}})$. The drawn level curves correspond to $Q(\widehat{E}_0,\,\widehat{\sigma}_0;\,\widehat{\mathbf{A}})+n^2$ with $n=1,\,2,\,\ldots,\,8$.

3.3. Uncertainty budget

Table 2 lists the relative uncertainties estimated for the parameters directly involved in the measurement of the DDCS at the maximum energy transfer point, equation (6). The fact that the uncertainty of the amplitude parameter A varies from 1.6% (at $\theta=35°$) to 6.0% (at $\theta=131°$) for the elements C and Al, and from 0.8% (at $\theta=35°$) to 4.0% (at $\theta=131°$) for Te, Ta and Au, is directly related to the counting statistics at each observation angle (see figure 6). It is important to stress that the uncertainties introduced in the net spectra by the bremsstrahlung produced in the C substrate, pile-up, and background corrections were propagated to the uncertainty associated with each channel count. So, these effects are incorporated in the fitting procedure and consequently in the final uncertainty of A.

The quadratic propagation of the uncertainties listed in table 2 fixes the final estimated uncertainty of the experimental DDCSs between the following limits: 5.5%–13% for C, 4.2%–13% for Al, 3.2%–6.5% for Te, 3.6%–7.2% for Ta and 2.5%–3.3% for Au. The largest uncertainties are for the measurements at 100 keV and 131° (13% in the case of C and Al).

4. Results

Table 3 presents the fitted values E_0 and σ_0 for each irradiation of each element along with the experimental DDCSs at $\kappa=1$ and the three measured angles. For the lightest elements, C and Al, 4 energies were studied. In turn, 11 energies were investigated for Te, Ta and Au. Our DDCSs span 5 orders of magnitude, from 10^{-2} to 10^{3} mb keV^{-1} sr^{-1}. The

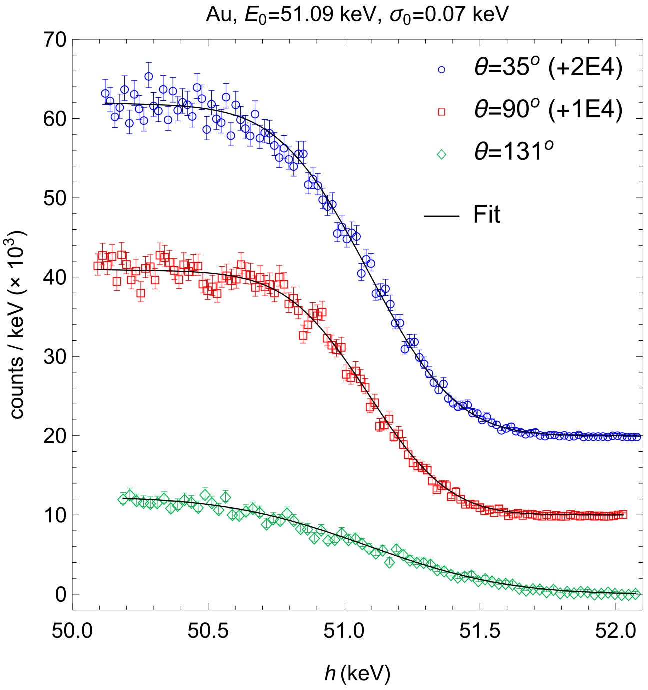

Figure 6. Experimental spectra at the tip region collected with the three detectors for the Au/C target, 51 keV run. The continuous curves represent the proposed tip spectrum model calculated with the fitted set $\widehat{\mathbf{A}}$.

Table 2. Main sources of uncertainty in the experimental DDCSs. The relative uncertainty values in % correspond to one standard deviation.

Quantity	Uncertainty (%)
Amplitude parameter, A	1.6–6.0 (C, Al) 0.8–4.0 (Te, Ta, Au)
Mean energy, E_0	<1
Number of incident electrons, N_0	<1
Atomic areal density, $\mathcal{N}t$	2.0–5.0
Solid angle, Ω	1.0

high stability of the electron gun and the narrow energy distribution of the beam are evident from the results of σ_0. Actually, according to the Gaussian hypothesis, the interval of width ~0.42 keV ($2 \times 3\sigma_0$, taking $\sigma_0 = 0.07$ keV) centered at E_0 contains more than 99.7% of the electron beam. This width represents 2% of the lowest studied energy, $E_0 = 20.38$ keV, while for $E_0 = 100.80$ keV this fraction decreases to 0.4%.

In order to make a direct comparison with the product of the scaled differential cross section $\chi(Z, E_0, E)$, tabulated by Seltzer and Berger [19], and the bremsstrahlung angular distribution $S(Z, E_0, E, \theta)$, tabulated by Kissel *et al* [15], we multiplied our experimental results by the factor $E_0\beta^2/Z^2$, considering the tip condition $E = E_0$. This scaling reveals the strong dependence of the product $\chi\, S$ with the photon emission angle and the electron kinetic energy (see figures 7–11). In the plots pertaining to Al and Au we include the values extracted from the tabulations of Seltzer and Berger [19] and Kissel *et al* [15], at 1, 2, 5, 10, 20, 50 and 100 keV (symbolized with plus signs). The continuous curves in figures 7–11 represent the interpolation derived from these nodes and are accompanied by a band containing the interval of ±11% associated with the theoretical uncertainty [15, 19].

5. Discussion

In general, two different behaviors are observed between $E_0 = 1$ keV and 100 keV. For the forward emission angle $\theta = 35°$, theory predicts a growing tendency of the product $\chi\, S$. The experimental points agree with the theoretical estimates within their respective uncertainties. In the case of Al and Au (figures 8(a) and 11(a)) the experimental error bars include the theoretical value within one or two standard deviations, whereas for C (figure 7(a)) the experiment is slightly higher than theory and for Te and Ta (figures 9(a) and 10(a)) somewhat lower.

Regarding the lateral and backward photon emission angles, theory foresees first an increase of $\chi\, S$ above $E_0 = 1$ keV, reaching a maximum between 2 and 20 keV, depending on the element, and a subsequent decrease for higher energies. At $\theta = 90°$, the measurements are in accord with the theoretical predictions except for Ta at $E_0 \geqslant 75$ keV, where the experimental DDCSs are below the theoretical uncertainty band (figure 10(b)). Similarly, at $\theta = 131°$ the experimental points are contained within the ±11% band apart from the DDCSs of Te and Ta with energies $E_0 \geqslant 60$ keV, which are below the lower limit of the theoretical uncertainty (figures 9(c) and 10(c)).

To get further insight into the observed trends, we calculated the ratio between the experimental and the theoretical DDCSs (figure 12). We fitted a constant function to these ratios, which is equivalent to compute the average value (black horizontal lines in the plots of figure 12 including its standard deviation). This procedure allows testing the hypothesis that the theoretical curve and the experimental points follow the same functional form with E_0, except for a constant factor.

The average ratios for C at the three angles are compatible within their uncertainties, indicating that the experiment is consistently about 10% higher than the theory. In the casse of Al, at $\theta = 35°$ and 90°, the fitted ratios are compatible with 1.00, but increase to 1.07 at $\theta = 131°$. Hence, for these two elements the fit is adequate according to the chi-square test; the hypothesis can therefore not be rejected. The same can be concluded for the ratios corresponding to $\theta = 35°$ and 90° in Te, Ta and Au, where the fitted values are around 0.90, 0.86 and 1.00, respectively. On the contrary, we reject the hypothesis for measurements at $\theta = 131°$. At this angle the ratios decrease with increasing E_0, and a linear regression is an acceptable model to describe the data (red line in the plots of Te, Ta and Au at $\theta = 131°$).

Table 3. Present electron bremsstrahlung DDCSs measured at $\kappa = 1$ and $\theta = 35°$, $90°$ and $131°$. The numbers between parentheses are the uncertainties (one standard deviation) in units of the least significant digit. The uncertainties in the adjusted values E_0 and σ_0 are around 0.01 keV.

			DDCS (mb keV^{-1} sr^{-1}) at $\kappa = 1$		
Element	E_0 (keV)	σ_0 (keV)	$\theta = 35°$	$\theta = 90°$	$\theta = 131°$
C	22.39	0.12	7.5(4)	7.9(4)	2.03(12)
	51.01	0.12	1.56(8)	0.89(5)	0.178(12)
	75.46	0.08	0.76(4)	0.294(17)	0.057(5)
	100.57	0.07	0.451(24)	0.120(10)	0.0184(24)
Al	20.38	0.08	56.5(25)	59.6(26)	18.6(9)
	50.96	0.10	10.2(5)	5.96(27)	1.34(8)
	75.57	0.07	5.25(25)	1.93(10)	0.39(3)
	100.48	0.07	3.47(17)	1.04(9)	0.171(23)
Te	22.57	0.08	665(23)	661(23)	334(12)
	27.38	0.08	487(17)	450(15)	207(7)
	31.77	0.08	388(13)	335(11)	140(5)
	41.56	0.10	262(9)	193(7)	70(3)
	51.19	0.07	193(6)	123(4)	43.5(14)
	61.10	0.07	146(5)	85(3)	23.1(9)
	70.74	0.07	117(4)	60.6(21)	15.9(6)
	75.71	0.06	110(3)	47.6(15)	14.4(5)
	80.61	0.06	99(3)	43.8(16)	11.3(5)
	90.72	0.10	86(3)	32.0(14)	8.0(5)
	100.73	0.07	74.2(23)	23.9(8)	6.18(22)
Ta	22.58	0.12	1206(47)	1293(50)	658(26)
	27.39	0.09	885(39)	902(15)	424(19)
	31.74	0.11	709(31)	675(29)	292(13)
	41.51	0.07	478(21)	381(17)	148(7)
	51.19	0.09	359(13)	248(3)	95(4)
	61.11	0.07	271(12)	171(7)	54.0(26)
	70.66	0.08	221(9)	126(5)	38.7(17)
	75.71	0.08	204(8)	100(4)	33.8(14)
	80.62	0.09	185(8)	91(4)	27.8(14)
	90.71	0.11	165(8)	67(3)	18.9(11)
	100.80	0.07	140(5)	48.8(19)	15.2(6)
Au	20.38	0.07	1871(46)	2119(52)	1059(27)
	25.02	0.07	1348(34)	1395(35)	680(19)
	27.00	0.08	1198(29)	1207(29)	583(15)
	31.67	0.07	946(23)	882(21)	414(10)
	41.52	0.06	644(16)	517(13)	212(5)
	51.09	0.07	474(11)	340(8)	132(3)
	60.88	0.08	373(9)	232(6)	80.5(25)
	70.57	0.06	297(7)	174(4)	58.8(17)
	75.68	0.07	274(7)	145(4)	50.2(13)
	90.31	0.08	220(5)	99.2(3)	31.5(10)
	100.48	0.05	189(5)	72.7(19)	21.3(7)

As a rule, the best agreement between experiment and theory was achieved for the measurements at $\theta = 35°$ and $90°$, especially in Al and Au. This is not unexpected if we recall that both elements are in the set of six elements for which Pratt *et al* [14] and Kissel *et al* [15] carried out partial-wave calculations. Although for C, Te and Ta we observed the same functional form with E_0 at these angles, the differences in absolute value might be attributed to the extrapolation (in κ) and interpolation (in Z and E_0) procedures employed to evaluate the theoretical DDCSs. Concerning the angle $\theta = 131°$, despite the discussed differences, the experimental points of Al and Au are well contained within the interval of ±11%. From these observations we infer that the uncertainty estimated by Seltzer and Berger [19] and Kissel *et al* [15] for the theoretical DDCSs at the tip is conservative for Al and Au and electrons with E_0 between 20 and 100 keV, and could be reduced to ±5%.

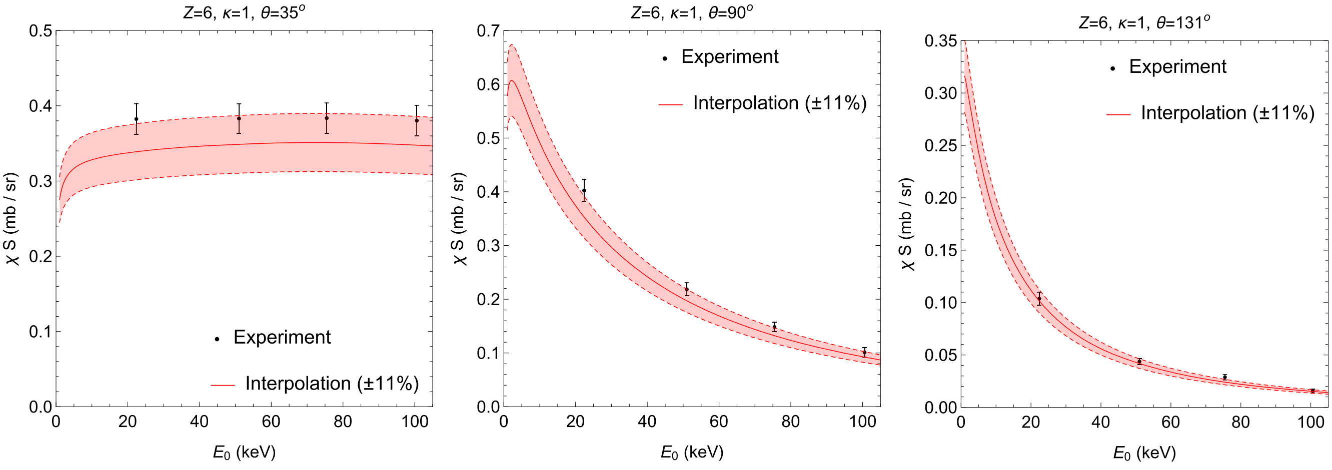

(a) (b) (c)

Figure 7. Experimental scaled DDCS, χS, for $Z = 6$ (C), $\kappa = 1$ and $\theta = 35°$, 90° and 131° (circles with error bars that correspond to one standard deviation), and interpolation from the calculation of Seltzer and Berger [19] and Kissel *et al* [15] (continuous curve) as a function of the electron kinetic energy.

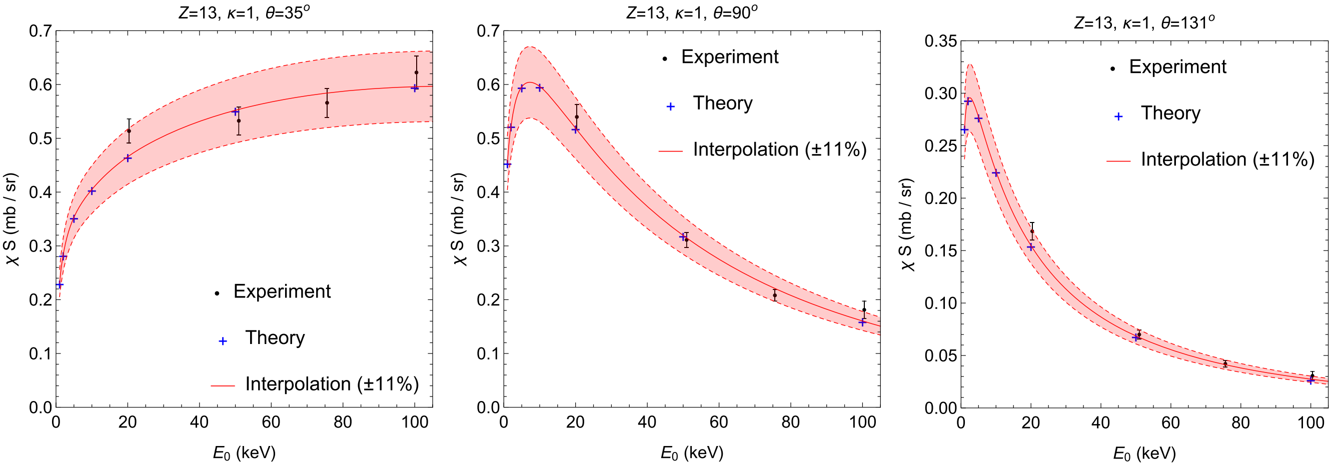

(a) (b) (c)

Figure 8. Experimental scaled DDCSs, χS, for $Z = 13$ (Al), $\kappa = 1$ and $\theta = 35°$, 90° and 131° (circles with error bars that correspond to one standard deviation), theoretical calculation of Seltzer and Berger [19] and Kissel *et al* [15] (plus symbols), and interpolation of the latter points (continuous curve) as a function of the electron kinetic energy.

6. Conclusions

We have measured a total of 123 absolute electron bremsstrahlung DDCSs at the tip of the spectrum for the elements C, Al, Te, Ta and Au, energies between 20 and 100 keV and three emission angles. A precise determination of the target thicknesses was achieved by RBS. The other quantities related to the experimental arrangement, such as the solid angle subtended by each detector with respect to the target position and the number of incident electrons, were measured with high accuracy too. The energy spread of the incident electron beam was modeled and obtained for each run from the three independently collected spectra. From this adjusted parameter we assessed the narrow energy distribution of the electron beam, which is essential to yield the DDCS at the tip.

The comparison of the theoretical calculation of Seltzer and Berger [19] and Kissel *et al* [15], with our experimental DDCS for Al and Au shows very good agreement. Interestingly, Al and Au were among the few elements for which partial-wave cross sections were actually calculated instead of interpolated (in Z). We believe that, for these elements, the relative uncertainty of the theoretical cross sections does not exceed 5% in the energy interval addressed in the present work. On the other hand, the estimate of ±11% seems to be adequate for C and Te, and might be greater for Ta.

Acknowledgments

We thank MSc W G P Engel and Professor A Domingues for preparing the targets, and also to the technical staffs of the

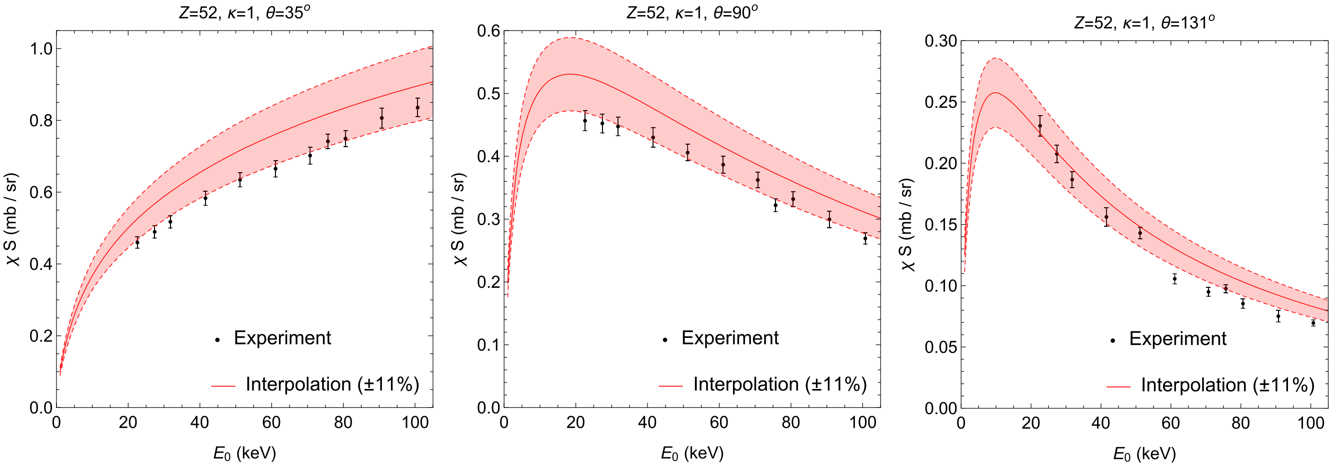

(a) (b) (c)

Figure 9. Same as figure 7 except that $Z = 52$ (Te).

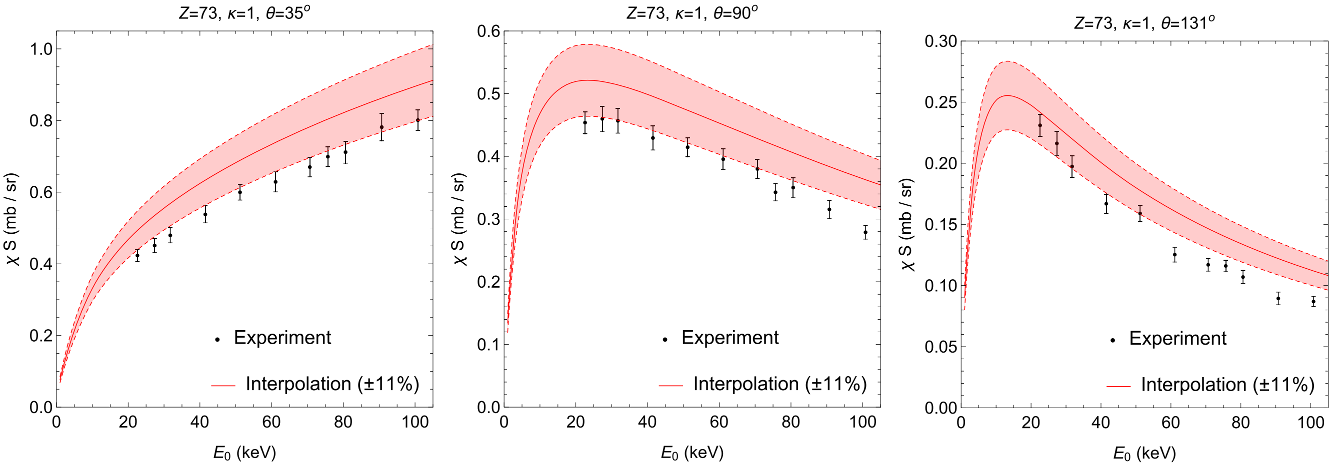

(a) (b) (c)

Figure 10. Same as figure 7 except that $Z = 73$ (Ta).

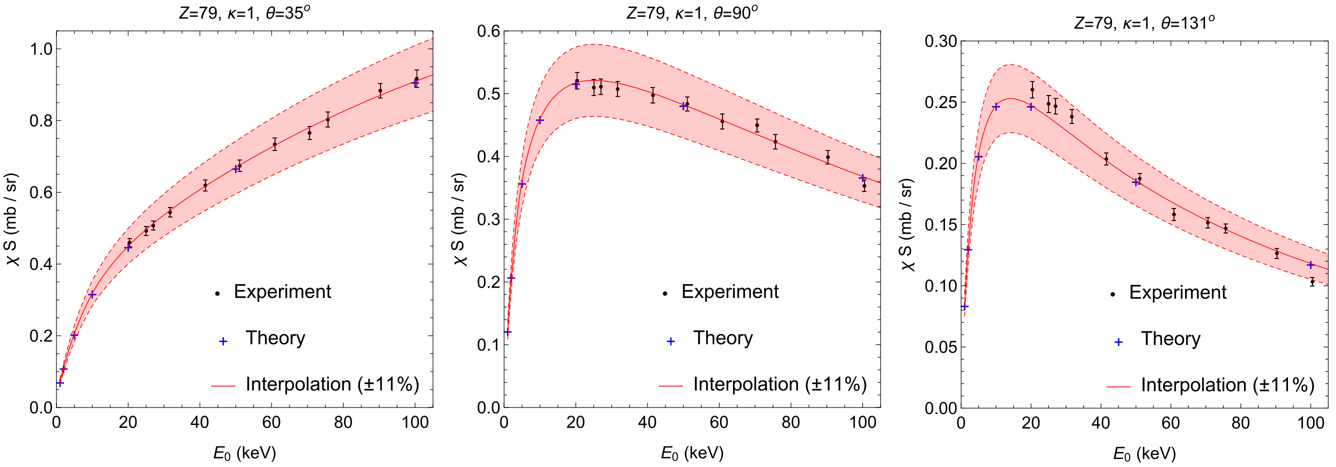

(a) (b) (c)

Figure 11. Same as figure 8 except that $Z = 79$ (Au).

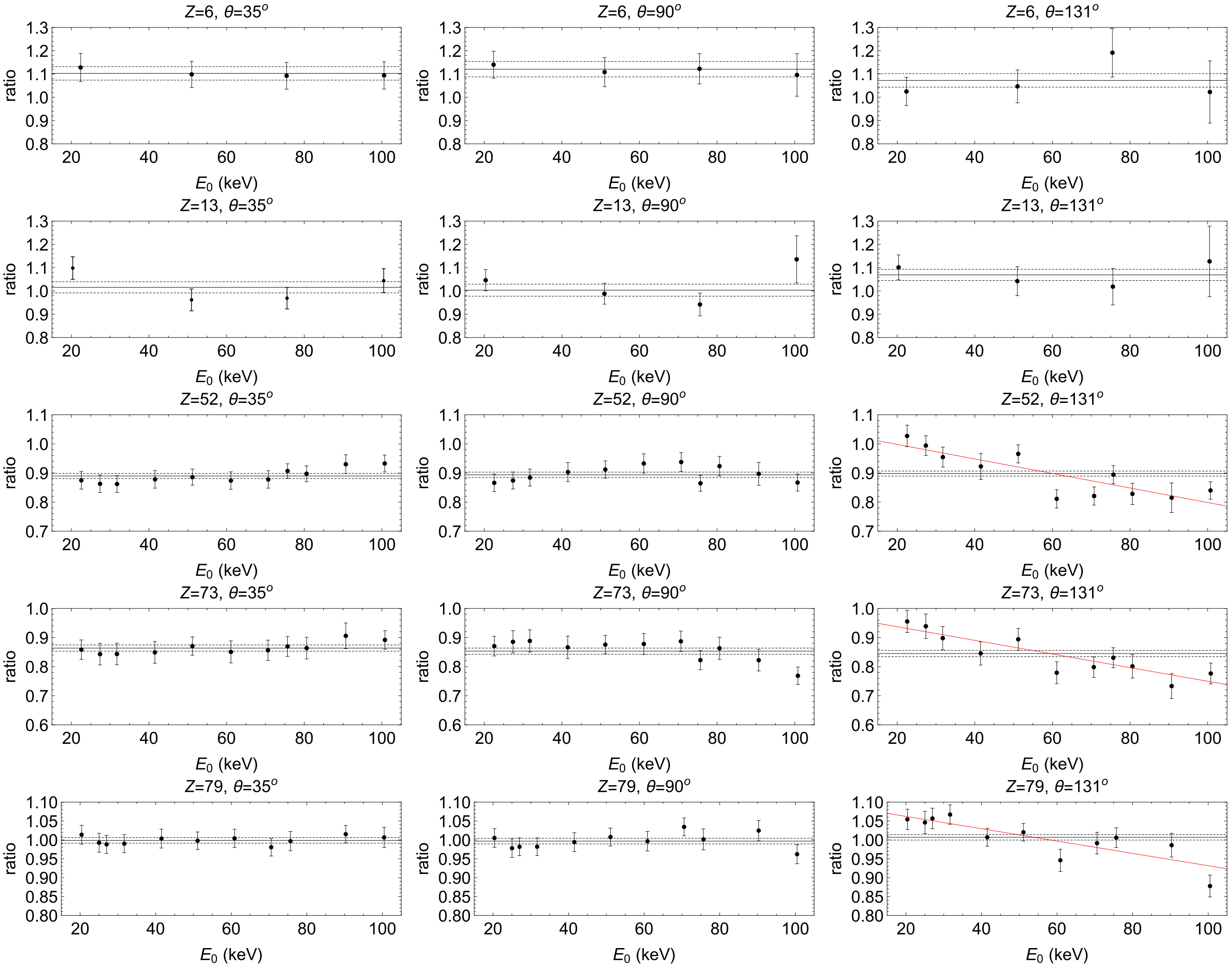

Figure 12. Ratios between experimental and theoretical DDCSs at the tip. The error bars include only the experimental uncertainty. The black horizontal lines indicate the average values and their standard deviations, while the red lines represent a linear fit.

São Paulo Microtron Accelerator and the LAMFI/IFUSP tandem van de Graaff Accelerator. We gratefully acknowledge the financial support of CNPq (Conselho Nacional de Pesquisas, Brazil), FAPESP (Fundação de Amparo à Pesquisa do Estado de São Paulo) and CAPES (Coordenação de Aperfeiçoamento de Pessoal de Ensino Superior, Brazil). JMF-V thanks the Universidade de São Paulo for a visiting professorship as well as the Generalitat de Catalunya (grant no. 2014 SGR 846).

Appendix A. Detector RF to analyze the *tip* region of the bremsstrahlung spectra

To quantify the deposited energy spectrum $D(\epsilon, E; \mathbf{g})$ the following components were addressed in [32]: (A) the full-energy absorption of photons, and the escape from the active volume of (B) Ge K x-rays, (C) photons after one Compton interaction, and (D) photo-electrons. The analytical RF includes external interaction contributions like the effects caused by (E) electrons produced in the Ge dead layer that reach the active volume, and (F) the incoherent scattering of photons in the detector window. Figure A1 displays the RF of the detector placed at $\theta = 90°$, for 50 keV photons.

In the RF, the main contributions to the incomplete energy deposition are the escape of Ge K x-rays (B) and scattered photons after Compton interactions (C). Notice that both structures are separated from the full-energy peak (A). Since the focus of this work is the maximum energy transfer point, we only need to analyze the interval within ~1 keV around the tip. The effects of components from (B)–(E) are outside the region of interest or are several orders of magnitude lower than the two relevant effects that will be considered, namely the full-energy peak (A) and the tail produced by photons that are scattered inelastically in the detector window (F). Hence, we calculated the RF of each detector as

$$\begin{aligned} R(h, E) = {} & T(E)\mathcal{G}(h, E; s)\, \varepsilon_{\mathrm{i}}(E; \mathbf{g}) \\ & + T'(E)\int_{E'_{\min}}^{E} \mathcal{G}(h, E'; s)\, P_{\mathrm{w}}(E, E'; \mathbf{g}) \\ & \times \varepsilon_{\mathrm{i}}(E'; \mathbf{g})\, \mathrm{d}E', \end{aligned} \tag{A.1}$$

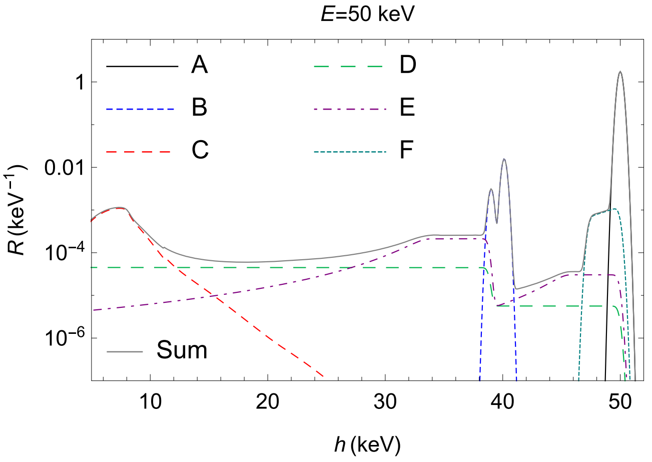

Figure A1. RF of the planar HPGe detector placed at $\theta = 90°$ for $E = 50$ keV. The plotted components are: (A) full-energy absorption peak, (B) Ge Kα and Kβ x-ray escape peaks, (C) photon escape after one Compton interaction, (D) photo-electron escape from the active volume, (E) photo-electrons generated in the Ge dead layer that reach the active volume, and (F) incoherent scattering of photons in the Be window.

where $\varepsilon_{\rm i}(E; \mathbf{g})$ is the intrinsic efficiency (equation (19) in [32]) whereas $P_{\rm w}(E, E'; \mathbf{g})$ describes the probability that the incident photon with energy E is scattered inelastically in the detector window and enters the active volume with a lower energy E' (equation (23) in [32]), having a probability $\varepsilon_{\rm i}(E'; \mathbf{g})$ of being absorbed. The lower integration limit $E'_{\rm min}$ depends on the detector geometry, equation (25) in [32]. The only difference between T and T' is that the latter disregards the attenuation in the detector window.

Although the RF model was originally developed for planar Ge detectors, only minor modifications were necessary to extend it to the coaxial configuration. In fact, just the Compton escape component (B) is slightly different in this case. Specifically, after a forward scattering this escape probability decreases owing to the increase in the active volume with respect to the planar configuration. Moreover, for $E \lesssim 100$ keV most of the interactions take place near the detector front surface and, as a consequence, the vast majority of particle escape processes occur there. Thus, the equations to describe these phenomena, which dominate in the RF, are the same for both planar and coaxial crystals. More details about the model extension can be found in [36].

Appendix B. The solid angle as a function of the incident photon energy

We consider a cylindrical collimator of length $d_{\rm c}$ and aperture radius $r_{\rm c}$. An isotropic photon emission point is placed at a distance $d_{\rm s}$ in the negative direction of the symmetry axis z (see figure B1).

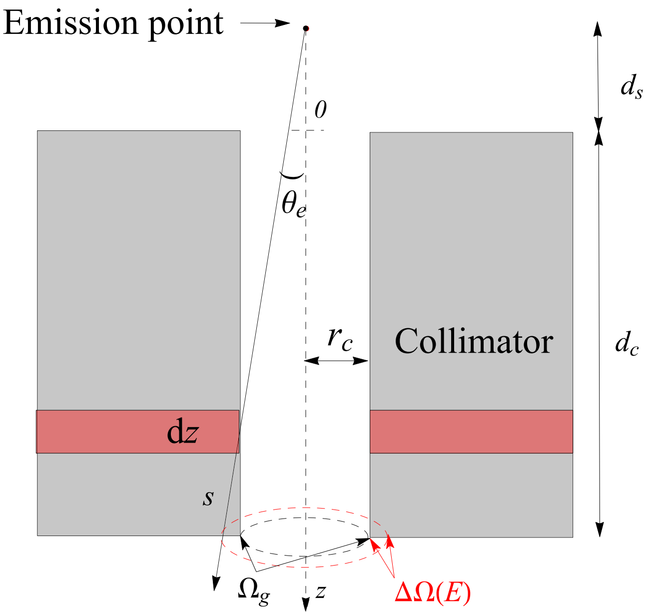

Figure B1. Two-dimensional scheme of the collimator and the photon emission point (not to scale). The origin of the coordinate system coincides with the intersection of the upper plane of the collimator and the symmetry axis.

The number of photons dN emitted towards the solid angle $\mathrm{d}\Omega = \mathrm{d}(\cos\theta_{\rm e})\mathrm{d}\phi_{\rm e}$ around the direction $(\theta_{\rm e}, \phi_{\rm e})$ is given by $\mathrm{d}N = \mathrm{d}\Omega/4\pi$, where $\theta_{\rm e}$ and $\phi_{\rm e}$ are the polar and the azimuthal angles, respectively. Due to the cylindrical symmetry of the set up, the number of photons emitted in the annular differential solid angle $\mathrm{d}\Omega = 2\pi\,\mathrm{d}(\cos\theta_{\rm e})$ is

$$\mathrm{d}N = \frac{1}{2}\,\mathrm{d}(\cos\theta_{\rm e}). \tag{B.1}$$

On the other hand, $\cos\theta_{\rm e}$ is related to the coordinate z of the collimator according to

$$\cos\theta_{\rm e} = \frac{z + d_{\rm s}}{\sqrt{r_{\rm c}^2 + (z + d_{\rm s})^2}}. \tag{B.2}$$

Then, the number of photons hitting the internal wall of the collimator at a depth between z and $z + \mathrm{d}z$ can be calculated by means of a change of variable (see figure B1):

$$\mathrm{d}N(z) = \frac{1}{2r_{\rm c}}\left[1 + \left(\frac{z + d_{\rm s}}{r_{\rm c}}\right)^2\right]^{-3/2}\mathrm{d}z. \tag{B.3}$$

From this expression and equation (B.1) one can deduce the geometrical solid angle $\Omega_{\rm g}$ defined by the internal wall of the collimator,

$$\Omega_{\rm g} = 4\pi\int_{d_{\rm c}}^{\infty}\mathrm{d}N(z), \tag{B.4}$$

and the effective increase of solid angle $\Delta\Omega(E)$ produced by the collimator transparency,

$$\Delta\Omega(E) = 4\pi\int_0^{d_{\rm c}}\mathrm{d}N(z)\exp\left[-\mu_{\rm Cu}(E)\,s(z)\right], \tag{B.5}$$

where $\mu_{\rm Cu}(E)$ is the linear attenuation coefficient of the material of the collimator (Cu in our case) and

$$s(z) = \frac{d_{\rm c} - z}{z + d_{\rm s}}\sqrt{r_{\rm c}^2 + (z + d_{\rm s})^2}. \tag{B.6}$$

Observe that $\Delta\Omega$ is given by the number of photons that penetrate the internal wall of the collimator and, after traveling the distance s, emerge from the final surface without interacting (see figure B1).

Finally, we define the effective solid angle Ω subtended by the detector with respect to the emission point as

$$\Omega = \Omega_{\mathrm{g}} + \Delta\Omega(E). \tag{B.7}$$

In the fit procedure described in section 2.4, we calculated $\Delta\Omega(E)$ for each measured energy E, and afterwards the common parameter Ω_{g} was fitted.

References

[1] Fano U, Koch H W and Motz J W 1958 *Phys. Rev.* **112** 1679
[2] Pratt R H 1960 *Phys. Rev.* **120** 1717
[3] Jabbur R J and Pratt R H 1963 *Phys. Rev.* **129** 184
[4] Hall H E, Hanson O and Jamnik D 1963 *Phys. Rev.* **129** 2207
[5] Jabbur R J and Pratt R H 1964 *Phys. Rev.* **133** B1090
[6] Elwert G and Haug E 1969 *Phys. Rev.* **183** 90
[7] Haug E 1974 *Phys. Lett.* A **49** 68
[8] Pratt R H and Tseng H K 1975 *Phys. Rev.* A **11** 1797
[9] Lee C M and Pratt R H 1975 *Phys. Rev.* A **12** 707
[10] Olsen H A and Maximon L C 1978 *Phys. Rev.* A **18** 2517
[11] Feng I J, Goldberg I B, Kim Y S and Pratt R H 1983 *Phys. Rev.* A **28** 609
[12] Bethe H A and Heitler W 1934 *Math. Proc. Cambridge Philos. Soc.* **30** 524
[13] Tseng H K and Pratt R H 1971 *Phys. Rev.* A **3** 100
[14] Pratt R H, Tseng H K, Lee C M, Kissel L, MacCallun C and Riley M 1977 *At. Data Nucl. Data Tables* **20** 175
[15] Kissel L, Quarles C A and Pratt R H 1983 *At. Data Nucl. Data Tables* **28** 381
[16] Lee C M, Kissel L, Pratt R H and Tseng H K 1976 *Phys. Rev.* A **13** 1714
[17] Tseng H K, Pratt R H and Lee C M 1979 *Phys. Rev.* A **19** 187
[18] Seltzer S M and Berger M J 1985 *Nucl. Instrum. Methods* B **12** 95
[19] Seltzer S M and Berger M J 1986 *At. Data Nucl. Data Tables* **35** 345
[20] Quarles C A 2000 *Radiat. Phys. Chem.* **59** 159
[21] Quarles C A and Portillo S 2006 *Radiat. Phys. Chem.* **75** 1187
[22] Starek B, Aiginger H and Unfried E 1972 *Phys. Lett.* A **39** 151
[23] Aehlig A, Scheer M and Zilker F 1975 *Phys. Lett.* A **51** 221
[24] Agostinelli S *et al* 2003 *Nucl. Instrum. Methods* A **506** 250
[25] Kawrakow I 2000 *Med. Phys.* **27** 485
[26] Salvat F, Fernández-Varea J M and Sempau J 2011 *PENELOPE: A Code System for Monte Carlo Simulation of Electron and Photon Transport* (Issy-les-Moulineaux: NEA/OECD)
[27] Faddegon B A, Asai M, Perl J, Ross C, Sempau J, Tinslay J and Salvat F 2008 *Med. Phys.* **35** 4308
[28] Pandola L, Andenna C and Caccia B 2015 *Nucl. Instrum. Methods* B **350** 41
[29] www2.if.usp.br/lamfi/ (Accessed: 14 October 2016)
[30] Silva T F, Rodrigues C L, Mayer M, Moro M V, Trindade G F, Aguirre F R, Added N, Rizzutto M A and Tabacniks M H 2016 *Nucl. Instrum. Methods* B **371** 86
[31] Mayer M 1999 *AIP Conf. Proc.* **475** 541
[32] García-Alvarez J A, Maidana N L, Vanin V R and Fernández-Varea J M 2016 *Radiat. Phys. Chem.* **121** 23
[33] Fernández-Varea J M, Jahnke V, Maidana N L, Malafronte A A and Vanin V R 2014 *J. Phys. B: At. Mol. Opt. Phys.* **47** 155201
[34] Vanin V R, Manso Guevara M V, Maidana N L, Martins M N and Fernández-Varea J M 2016 *Radiat. Phys. Chem.* **119** 14
[35] Barros S F, Vanin V R, Maidana N L and Fernández-Varea J M 2015 *J. Phys. B: At. Mol. Opt. Phys.* **48** 175201
[36] García-Alvarez J A 2016 *Electron bremsstrahlung cross sections, experimental study in the São Paulo Microtron Accelerator* (Universidade de São Paulo, in Portuguese) http://teses.usp.br/teses/disponiveis/43/43134/tde-30112016-095354/en.php